

Atomistic insight into ordered defect superstructures at novel grain boundaries in CuO nanosheets: From structures to electronic properties

Lulu Zhao¹, Lei Li¹, Huaping Sheng¹, He Zheng¹ (✉), Shuangfeng Jia¹, Weiwei Meng¹, Huihui Liu¹, Fan Cao¹, Huayu Peng¹, and Jianbo Wang^{1,2} (✉)

¹ School of Physics and Technology, Center for Electron Microscopy, MOE Key Laboratory of Artificial Micro- and Nano-structures, and Institute for Advanced Studies, Wuhan University, Wuhan 430072, China

² Science and Technology on High Strength Structural Materials Laboratory, Central South University, Changsha 410083, China

© Tsinghua University Press and Springer-Verlag GmbH Germany, part of Springer Nature 2019

Received: 29 December 2018 / Revised: 17 February 2019 / Accepted: 20 February 2019

ABSTRACT

Determining atomistic structures of grain boundaries (GBs) is essential to understand structure–property interplay in oxides. Here, different GB superstructures in CuO nanosheets, including (11 $\bar{1}$) and (114) twinning boundaries (TBs) and (002)/(223) GB, are investigated. Unlike the lower-energy stoichiometric (11 $\bar{1}$) TB, both experimental and first-principles investigations reveal a severe segregation of Cu and O vacancies and a nonstoichiometric property at (114) TB, which may facilitate ionic transportation and provide space for elemental segregation. More importantly, the calculated electronic structures have shown the increased conductivity as well as the unanticipated magnetism in both (114) TB and (002)/(223) GB. These findings could contribute to the race towards the property-directing structural design by GB engineering.

KEYWORDS

grain boundaries, atomistic structure, electronic property, scanning transmission electron microscopy (STEM), first-principles

1 Introduction

Transition metal oxides have been proved to be the ideal low-cost materials for energy, electronic, and catalytic applications, such as the electrodes in ion batteries [1–3] dielectric materials for capacitors [4], etc. [5–8]. The property-directing structural design is a prerequisite for achieving success in these endeavors, which involves the complicated electron design principles [9–15]. For example, the basic roadblock to enhance the energy conversion and storage efficiency lies in most cases in finding or designing the pathways that facilitate electron and ion transportations. One design avenue that has flourished recently is to control the symmetry and atomic structure at interfaces [16,17]. Success in these endeavors requires a range of electron design principles, which depends on correlating the structures with electronic properties.

Grain boundaries (GBs) are common interfaces in crystals. No matter naturally occurring or artificially fabricated, the GB could affect the physical and chemical properties [18–23], especially in low-dimensional materials. For instance, the GBs have been shown to effectively tune the catalytic performance and the dielectric constant in CuO nanomaterials [4, 24]. Moreover, solute decoration at GB leads to nanoscale chemical variations that can alter a material's performance by orders of magnitude (e.g., electrical transport property and embrittlement) [25–29]. Therefore, it is essential to clarify the nature of the GBs at the atomic scale to understand the structure–property interplay.

CuO is a typical transition-metal oxide with the low-symmetry monoclinic structure. Different GBs including the low-energy (11 $\bar{1}$), (002), (110), and (20 $\bar{2}$) twinning boundaries (TBs) were reported in CuO nanowires [30]. In our recent work, two-dimensional

nanosheets with (11 $\bar{1}$) TB and unreported high energy (114) TB and (002)/(223) GB have been successfully synthesized [31]. On the materials side, new interfaces may pose crucial challenges and provide new opportunities. However, the atomic-scale structures as well as the structure–property relationships regarding different GBs in CuO are currently lacking, which is the major roadblock for the potential applications.

Herein, using aberration-corrected scanning transmission electron microscopy (STEM) and electron energy-loss spectroscopy (EELS), combined with first-principles calculations, we studied the atomic superstructures and relative stability of the (11 $\bar{1}$) TB, (114) TB, and (002)/(223) GB. Both Cu and O sublattices of the GBs have been determined, based upon which the distinct electrical and magnetic properties in three different GBs were investigated.

2 Results and discussion

The high-angle annular dark-field (HAADF) and annular bright-field (ABF) images of (11 $\bar{1}$) TB along [1 $\bar{1}$ 0] projection are displayed in Figs. 1(a) and 1(b), which are consistent with the simulated images using the QSTEM software [32] shown in Figs. 1(c) and 1(d), respectively. The atomic models for image simulation are optimized based on the density functional theory (DFT) calculations (Fig. S1 in the Electronic Supplementary Material (ESM)). The TB comprises of repeated structural units as marked by polygons. In the HAADF image, the bright spots correspond to the Cu column locations, while the O columns are barely visible due to the small atomic number. Nevertheless, the oxygen columns can be directly identified in the ABF image, even in the TB core region, as indicated by the red arrows in Fig. 1(b). Both Cu and O atoms at the TB are fourfold

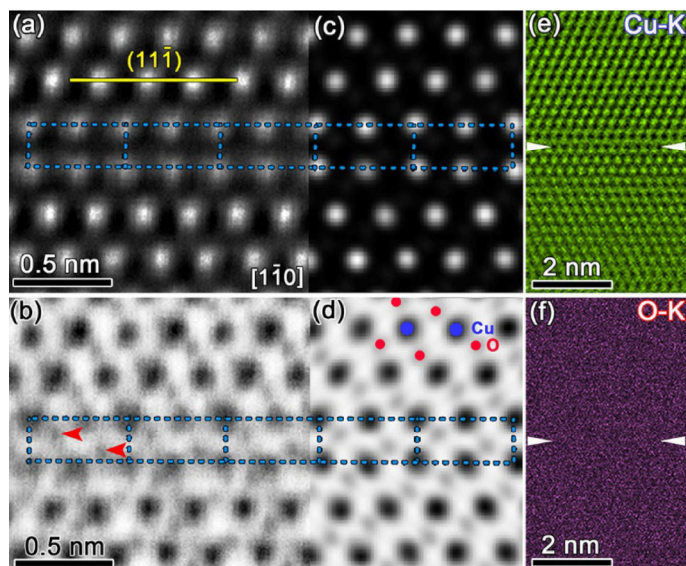


Figure 1 Atomistic structure of (111) TB. (a) HAADF and (b) ABF images of (111) TB taken along $[1\bar{1}0]$. The oxygen columns are indicated by red arrows in (b) and the structural units are shown by polygons. (c) Simulated HAADF and (d) simulated ABF images using the optimized TB structure by DFT calculations. (e) and (f) STEM-EDS elemental mappings of Cu-K and O-K, respectively, the TB core locations in which are indicated between white arrows.

coordinated without the existence of dangling bond, the same with that in bulk CuO. Only bond angles of atoms at the TB are slightly different from those in bulk as displayed in the detailed TB structure (Fig. S1(a) in the ESM), leading to the relatively lower free energy of (111) TB, ~ 0.49 J/m² (Table 1). Furthermore, the elemental mappings by the STEM energy-dispersive X-ray spectroscopy (EDS) show a uniform distribution of both Cu and O atoms across the TB into the grains (Figs. 1(e) and 1(f)).

Meanwhile, the atomistic superstructure formed at the (114) TB is much more complicated than that of (111) TB, which makes the O columns less evident in the ABF image (Fig. 2(b)). There are threefold coordinated Cu and O atoms at the (114) TB (Fig. S1(b) in the ESM). Thus, there exist dangling bonds of Cu and O as well as bond angle deviations, resulting in the relatively higher free energy of the (114) TB (~ 1.31 J/m² (Table 1)) which is less stable

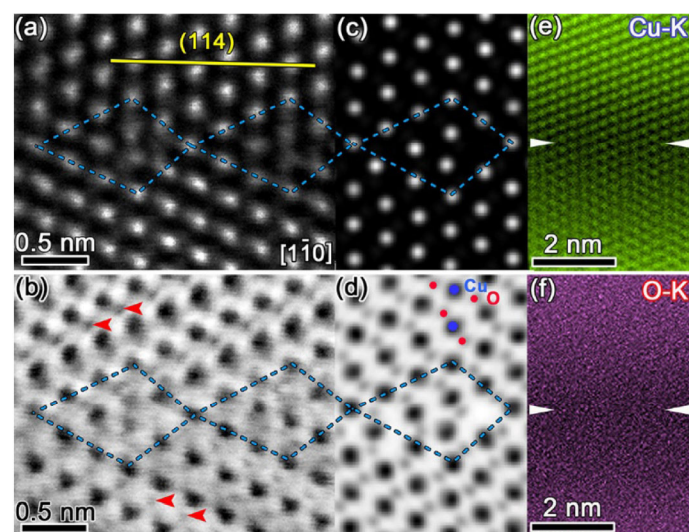


Figure 2 Atomistic structure of (114) TB. (a) HAADF and (b) ABF images of (114) TB taken along $[1\bar{1}0]$. The oxygen columns are indicated by red arrows in (b) and the structural units are shown by polygons. (c) Simulated HAADF and (d) simulated ABF images using the optimized TB structure by DFT calculations. (e) and (f) STEM-EDS elemental mappings of Cu-K and O-K respectively, the TB core locations in which are indicated between white arrows.

Table 1 Free energies of (111) TB, (114) TB and (002)/(223) GB

Grain boundary	Free energy (J/m ²)
(111) TB	0.49
(114) TB	1.31
(002)/(223) GB	2.05

than (111) TB. Moreover, in contrast to the uniform distribution at the (111) TB, a severe deficiency of Cu and O elements is evident in the (114) TB, as displayed in the elemental mappings by the STEM-EDS (Figs. 2(e) and 2(f)). Absolute thickness measurement shows a uniform thickness across (114) TB (Fig. S2 in the ESM) [33], excluding the influence of thickness on the deficiency of Cu and O elements. For comparison, the superstructure nucleated at the (002)/(223) GB is the most complicated one (Fig. S3 in the ESM) with a small lattice misfit as well as dangling bonds and bond angle deviation (Fig. S1(c) in the ESM), resulting in the highest interface free energy of 2.05 J/m² (Table 1) among these three kinds of GBs. Hence, it is reasonable to declare that the (002)/(223) GB and (114) TB with relatively higher free energies cannot be easily fabricated at the lower growth temperature of CuO (400–700 °C) as reported in Ref. [31].

It is well-documented that CuO exhibits the inherent p-type semiconducting property as induced by the occurrence of V_{Cu} [34,35], which may segregate at GBs [36–38]. This can be well illustrated by the periodic dark Z-contrast along the (114) TB (Fig. S4(a) in the ESM), implying a heavily insufficient occupations of Cu ions at certain sites as proved by the relatively lower intensity of Cu signal shown in the STEM-EDS elemental mappings (Figs. 2(e) and 2(f)). However, as mentioned above, few V_{Cu} exist at the (111) TB (Figs. 1(e) and 1(f)), indicated by the uniform elemental distribution. To understand this phenomenon from perspective of energetics, E_{seg} values of V_{Cu} and V_O at different sites in TBs were calculated using the relation $E_{seg} = E_V - E_{GB}$ [36], where E_V and E_{GB} are total free energies of the optimized supercell with and without one vacancy, respectively. The selected V_{Cu} and V_O sites at TBs and their corresponding segregation energies are displayed in Figs. 3(a)–3(d). The E_{seg} values of sites “3” at (111) TB and sites “6” at (114) TB are defined as the references (0 eV), correspondingly. A lower E_{seg} facilitates the formation of vacancy. For the (111) TB, the average E_{seg} for V_{Cu} and V_O are -0.32 and -0.21 eV, respectively (Fig. 3(b)). In contrast, for the (114) TB, the average E_{seg} for V_{Cu} and V_O are -0.95 and -0.76 eV (Fig. 3(d)), indicating that the vacancies are preferable to segregate in (114) TB (Fig. S4 in the ESM) which will relief the higher free energy at (114) TB mentioned above. Consequently, the E_{seg} value at site “3”, where Cu atom is threefold coordinated with bond angles around 120° deviating from fourfold coordinated Cu atoms in bulk with bond angles around 90° , is much lower, in well agreement with the relative weaker intensities at the same site (Figs. 3(e) and 3(f)).

Besides, it is speculated that more V_{Cu} may accumulate at the (114) TB than V_O due to its lower average E_{seg} , leading to a non-stoichiometric TB. To verify this, quantitative EELS analysis of the Cu L_3/L_2 ratio was conducted. The EELS spectra recorded across (111) and (114) TBs keep similar profiles (Figs. 4(a) and 4(b)). Inside the grains (3 nm from both TBs), the L_3/L_2 intensity ratio is calculated to be around 3.08 (Fig. 4(c)) which reaches maximum at the (114) TB (see EELS processing methods in the ESM). The discrepancy of this value from 3.5 obtained in Ref. [39] may originate from different step function used in calculations (see the ESM) and different experimental resolutions. Considering that the Cu- L_2 line is much smaller than Cu- L_3 line, the L_3/L_2 ratio should depend on experimental resolutions (1 eV in this work and 4 eV in Ref. [39]) [40]. In contrary, the L_3/L_2 ratio at (111) TB keeps consistent with the bulk ratio. Based on the previous studies,

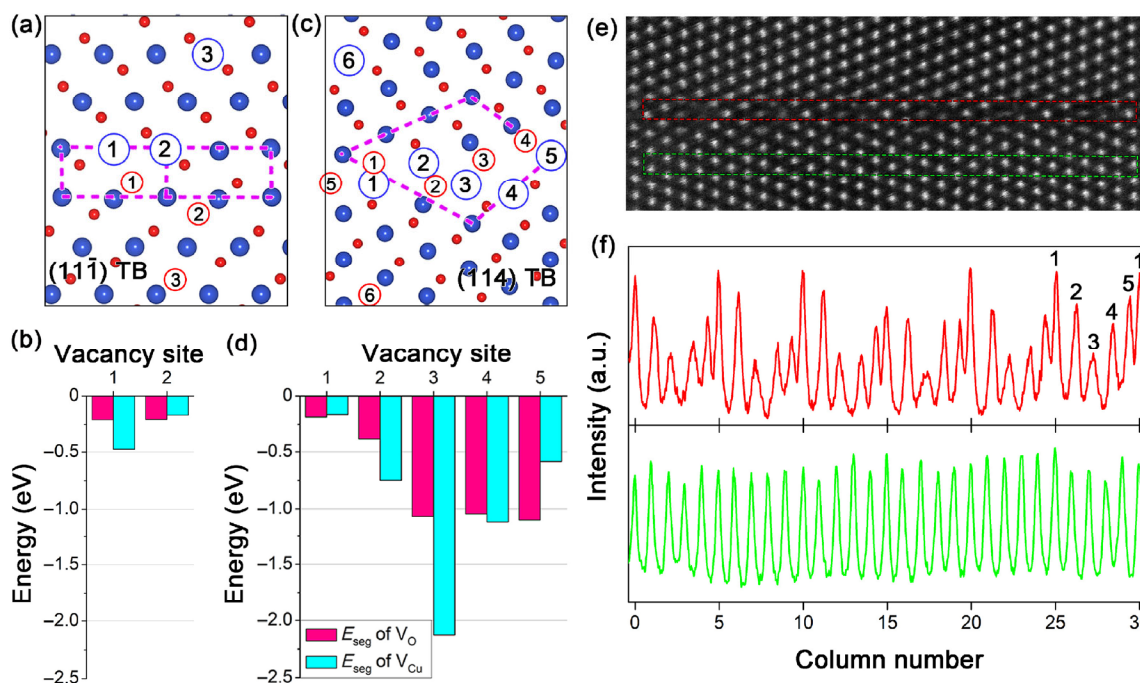


Figure 3 Vacancy segregation at $(11\bar{1})$ and (114) TBs. Atomic configuration with V_{Cu} and V_O at inequivalent sites for (a) $(11\bar{1})$ TB and (c) (114) TB. The blue and red circles represent selected sites for V_{Cu} and V_O , respectively. Relative E_{seg} of V_{Cu} and V_O for (b) $(11\bar{1})$ TB and (d) (114) TB. The E_{seg} of sites “3” and “6” are defined as reference (0 eV) for $(11\bar{1})$ TB and (114) TB, respectively. (e) HAADF image of (114) TB. (f) Intensity profiles obtained in dashed-boxed regions in (e), indicating the distribution of Cu atoms at the TB (red curve) and inside the grain (green curve). Obviously, the intensities of sites “1”–“5” shown at TB are well-predicted based on the corresponding E_{seg} values in (d) (blue columns).

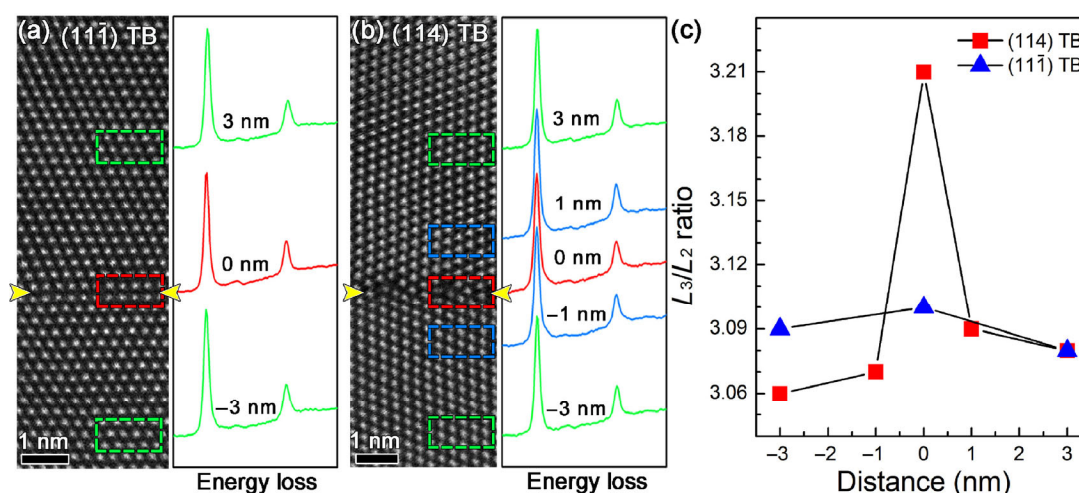


Figure 4 HAADF image (left) and corresponding EELS profiles of Cu- $L_{2,3}$ edge (right) recorded across (a) $(11\bar{1})$ TB and (b) (114) TB. (c) L_3/L_2 intensity ratios obtained based on those EELS profiles.

L_3/L_2 ratio reaches a maximum with approximately half filling of 3d states (d^5) and decreases or increases in occupation will reduce this ratio [41, 42]. This implies the less 3d states occupation in Cu ions at (114) TB and the existence of Cu ion with higher oxidation state, such as Cu^{3+} , and verifies the non-stoichiometric property and more severe segregation of V_{Cu} at (114) TB. The loose atomic structure at (114) TB will facilitate ionic transportation and may be applied to improve the electrochemical performance when CuO is employed as ion-battery anode materials [16]. Moreover, the large number of vacancies at GB provide spaces for the local decoration of solutes [25, 26]. It should be noted that the superstructure remains quite stable under the long-period (up to minutes) e-beam irradiation when taking the HAADF and ABF images, suggesting that e-beam should have negligible effects on the nucleation of superstructure. However, with the accumulation of irradiation dose, the intrinsic Cu less (114) TB gradually become an O less TB,

reflected in the occurrence of Cu^+ peak in EELS shown in Figs. S8(a) and S8(b) in the ESM. The similar phenomenon was observed at the stoichiometric $(11\bar{1})$ TB (Figs. S8(c) and S8(d) in the ESM). Theoretically, for 200 keV e-beam, the maximum energies (T_m) transferred to Cu and O are 8.2 and 32.8 eV. Compared with the calculated displacement energies E_d of 110.0 and 11.2 eV for Cu and O in CuO using DFT theory, the continuous e-beam irradiation will decrease the oxygen contents at the TB, consistent with the experimental observations (Fig. S8 in the ESM).

To gain more insights into the impact of GBs on electronic properties, we show the electronic structures of the three GBs obtained using their fully optimized geometries in Fig. 5 and Fig. S5 in the ESM. CuO is an intrinsically p-type semiconductor with a bandgap (E_g) of 1.2–1.9 eV [43–45] and the value calculated in this work is 1.2 eV (see the gray background in Fig. 5(a)). For the $(11\bar{1})$ TB, the Fermi level (E_F) lies in a gap, splitting the filled O 2p

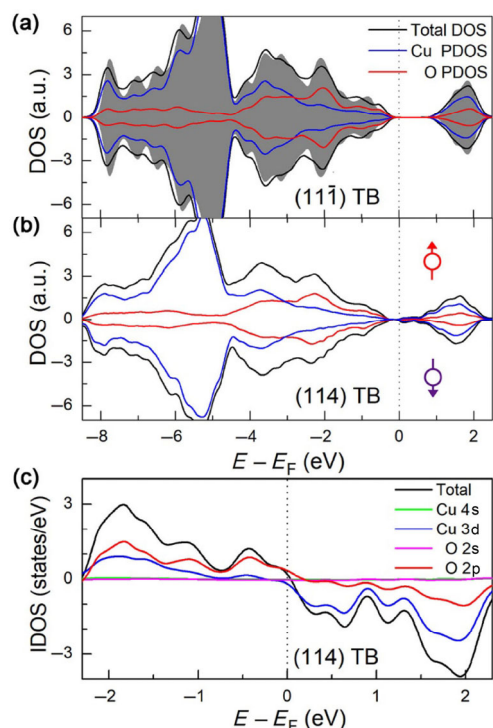


Figure 5 Electronic structures of (111) and (114) TBs. Total DOS and PDOS plots for (a) (111) TB and (b) (114) TB. The total DOS of CuO bulk is given in (a) as gray background. (c) Magnetic property of (114) TB shown by sum of IDOS and the contributions by Cu and O orbitals shown by sum of integrated Im-decomposed PDOS. The Fermi levels are set to zero and represented by vertical dashed lines.

orbitals from the unfilled Cu 3d orbitals. Meanwhile, the low-lying Cu 3d levels reduce the E_g to 0.62 eV (Fig. 5(a)). For the (002)/(223) GB, the E_g is closed by the planar defect (Fig. S5(a) in the ESM). For the (114) TB, the low-lying bands from the conduction band maximum (CBM) dominate density of states (DOS) around E_F (Fig. 5(b)). It is worth noting that a slight asymmetry between the spin up and spin down parts of DOS exists around the E_F in Fig. 5(b) and Fig. S5(a) in the ESM indicating the occurrence of net magnetic moments at (114) TB and (002)/(223) GB. Compared with the zero net magnetic moments in bulk CuO material and (111) TB, it is believed that the different coordination environment of transitional metal and oxygen atoms, i.e. threefold coordinated Cu and O atoms, will change the hybridization between Cu d and O p orbitals and thus lead to the appearance of net magnetic moments [46, 47]. To further investigate the magnetism in GB and its orbital contributions, the sum of integrated m-decomposed total DOS (IDOS) and sum of the integrated Im-decomposed atom-projected partial DOS (PDOS) for Cu and O in (114) TB and (002)/(223) GB are shown in Fig. 5(c) and Fig. S5(b) in the ESM. It is evident that the net magnetic moments mainly come from 2p orbitals of O below E_F and 3d orbitals of Cu above E_F and for (114) TB, the net magnetic moments show opposite directions below and above E_F . This phenomenon gives us the inspiration of the possibility to control the magnetic moment direction at GB through electron and hole doping and may be used in magnetic memory devices. The results show the novel influence of those abnormal superstructure GB structure to the transport and magnetic properties of materials, which may be important to realize functional devices through GB engineering.

3 Conclusions

In summary, the Cu and O sublattices have been determined in

three typical CuO GBs with the occurrence of novel ordered superstructures, based on which the atomic models for different GBs were established for the first-principles calculations. Unlike the stoichiometric (111) TB, a heavy segregation of the V_{Cu} and V_O at (114) TB has been shown at nonstoichiometric (114) TB, which can be well-interpreted based on the segregation energies of V_{Cu} and V_O . Further quantitative analysis of EELS spectra confirms this nonstoichiometric property. Meanwhile, it is theorized that the superstructure increases electrical conductivity and induces net magnetic moments at (114) TB and (002)/(223) GB. Our results may facilitate the comprehensive understanding of the structure–property relationships of GBs in CuO, which are likely to be used by electrical and chemical engineers for functionalizing the GBs in metal oxides.

4 Experimental

4.1 TEM characterizations

Our HAADF and ABF images were taken inside the Cs-corrected TEM (JEOL, JEM ARM200F) under high voltage of 200 kV. The raw EELS spectra were obtained under high voltage of 80 kV. Detailed data processing for EELS could be found in the ESM.

4.2 Theoretical calculations

Our first-principles calculations were performed with DFT using projector augmented wave within PBE+U, implemented by Vienna *ab-initio* simulation package (VASP) [48, 49]. A 450 eV plane-wave cutoff, Monkhorst-Pack k-point grid of $3 \times 3 \times 1$ for (111) and $3 \times 2 \times 1$ for (114) TB and (002)/(223) GB, and a U_{eff} of 7 eV [50] were used. Since the bulk CuO has an antiferromagnetic ground state, spin-polarization was considered in all cases. For the unit cell, magnetic moments of Cu atoms were set to be parallel with each other within the (100) planes [51]. Because the related magnetic properties of GBs should be notably altered due to the breaking symmetry, a stable magnetic configuration, where the magnetic moments of Cu atoms are parallel with each other within the (002) planes along $[1\bar{1}0]$, was used in all GB calculations. Atoms were fully relaxed until the residual forces are less than 0.05 eV/Å.

The initial atomic GB configurations are constructed based on HAADF and ABF images. The supercells contain 240–360 atoms and two equivalent GBs at the center and edges, distance between which is greater than 20 Å to minimize the interaction. A typical constructed supercell of (111) TB is shown in Fig. S6 in the ESM. To study the relative stability of different GBs, the GB free energies (γ) were further calculated by $\gamma = (E_{GB} - E_{Bulk})/2A$, where E_{GB} is the total free energy of supercell, E_{Bulk} is the total free energy in bulk, and A is the boundary area in one supercell.

Acknowledgements

This work was supported by the National Natural Science Foundation of China (Nos. 51671148, 51271134, J1210061, 11674251, 51501132, and 51601132), the Hubei Provincial Natural Science Foundation of China (Nos. 2016CFB446 and 2016CFB155), the Fundamental Research Funds for the Central Universities, the CERS-1-26 (CERS-China Equipment and Education Resources System), the China Postdoctoral Science Foundation (No. 2014T70734), the Open Research Fund of Science and Technology on High Strength Structural Materials Laboratory (Central South University), and the Suzhou Science and Technology project (No. SYG201619).

Electronic Supplementary Material: Supplementary material (EELS processing methods and additional figures) is available in the online version of this article at <https://doi.org/10.1007/s12274-019-2354-3>.

References

- [1] Liu, H. H.; Zheng, H.; Li, L.; Jia, S. F.; Meng, S.; Cao, F.; Lv, Y. H.; Zhao, D. S.; Wang, J. B. Surface-coating-mediated electrochemical performance in CuO nanowires during the sodiation-desodiation cycling. *Adv. Mater. Interfaces* **2018**, *5*, 1701255.
- [2] Assat, G.; Tarascon, J. M. Fundamental understanding and practical challenges of anionic redox activity in Li-ion batteries. *Nat. Energy* **2018**, *3*, 373–386.
- [3] Liu, H. H.; Cao, F.; Zheng, H.; Sheng, H. P.; Li, L.; Wu, S. J.; Liu, C.; Wang, J. B. *In situ* observation of the sodiation process in CuO nanowires. *Chem. Commun.* **2015**, *51*, 10443–10446.
- [4] Thongbai, P.; Maensiri, S.; Yamwong, T. Effects of grain, grain boundary, and dc electric field on giant dielectric response in high purity CuO ceramics. *J. Appl. Phys.* **2008**, *104*, 036107.
- [5] Twilton, J.; Le, C.; Zhang, P.; Shaw, M. H.; Evans, R. W.; MacMillan, D. W. The merger of transition metal and photocatalysis. *Nat. Rev. Chem.* **2017**, *1*, 0052.
- [6] Feng, Y. Z.; Zheng, X. L. Plasma-enhanced catalytic CuO nanowires for CO oxidation. *Nano Lett.* **2010**, *10*, 4762–4766.
- [7] Lu, L.; Yan, X.; Wang, J. B.; Zheng, H.; Hu, X. Y.; Tang, Y. W.; Jia, Z. Y. Oriented NiO nanosheets with regular hexagonal nanopores. *J. Phys. Chem. C* **2012**, *116*, 14638–14643.
- [8] Luo, L. J.; Lv, G.; Li, B. H.; Hu, X. Y.; Jin, L.; Wang, J. B.; Tang, Y. W. Formation of aligned ZnO nanotube arrays by chemical etching and coupling with CdSe for photovoltaic application. *Thin Solid Films* **2010**, *518*, 5146–5152.
- [9] Zheng, H.; Wang, J.; Huang, J. Y.; Wang, J. B.; Zhang, Z.; Mao, S. X. Dynamic process of phase transition from wurtzite to zinc blende structure in InAs nanowires. *Nano Lett.* **2013**, *13*, 6023–6027.
- [10] Wu, S. J.; Cao, F.; Zheng, H.; Sheng, H. P.; Liu, C.; Liu, Y.; Zhao, D. S.; Wang, J. B. Fabrication of faceted nanopores in magnesium. *Appl. Phys. Lett.* **2013**, *103*, 243101.
- [11] Jia, S. F.; Zheng, H.; Sang, H. Q.; Zhang, W. J.; Zhang, H.; Liao, L.; Wang, J. B. Self-assembly of K_xWO_3 nanowires into nanosheets by an oriented attachment mechanism. *ACS Appl. Mater. Interfaces* **2013**, *5*, 10346–10351.
- [12] Zhou, J. P.; Zhao, D. S.; Wang, R. H.; Sun, Z. F.; Wang, J. B.; Gui, J. N.; Zheng, O. *In situ* observation of ageing process and new morphologies of continuous precipitates in AZ91 magnesium alloy. *Mater. Lett.* **2007**, *61*, 4707–4710.
- [13] Tang, Y. W.; Jia, Z. Y.; Jiang, Y.; Li, L. Y.; Wang, J. B. Simple template-free solution route for the synthesis of $Ni(SO_4)_{0.5}(OH)_{1.4}$ nanobelts and their thermal degradation. *Nanotechnology* **2006**, *17*, 5686–5690.
- [14] Jang, H. W.; Ortiz, D.; Baek, S. H.; Folkman, C. M.; Das, R. R.; Shafer, P.; Chen, Y. B.; Nelson, C. T.; Pan, X. Q.; Ramesh, R. et al. Domain engineering for enhanced ferroelectric properties of epitaxial (001) BiFeO thin films. *Adv. Mater.* **2009**, *21*, 817–823.
- [15] Wang, J. B.; Li, L. Y.; Xiong, D. X.; Wang, R. H.; Zhao, D. S.; Min, C. P.; Yu, Y.; Ma, L. L. High spatially resolved morphological, structural and spectroscopic studies on copper oxide nanocrystals. *Nanotechnology* **2007**, *18*, 075705.
- [16] Nie, A. M.; Gan, L. Y.; Cheng, Y. C.; Li, Q. Q.; Yuan, Y. F.; Mashayek, F.; Wang, H. T.; Klie, R.; Schwingschlogl, U.; Shahbazian-Yassar, R. Twin boundary-assisted lithium ion transport. *Nano Lett.* **2015**, *15*, 610–615.
- [17] Moriwake, H.; Kuwabara, A.; Fisher, C. A. J.; Huang, R.; Hitosugi, T.; Ikuhara, Y. H.; Oki, H.; Ikuhara, Y. First-principles calculations of lithium-ion migration at a coherent grain boundary in a cathode material, LiCoO₂. *Adv. Mater.* **2013**, *25*, 618–622.
- [18] Long, H.; Fang, G. J.; Li, S. Z.; Mo, X. M.; Wang, H. N.; Huang, H. H.; Jiang, Q. K.; Wang, J. B.; Zhao, X. Z. A ZnO/ZnMgO multiple-quantum-well ultraviolet random laser diode. *IEEE Electron Dev. Lett.* **2011**, *32*, 54–56.
- [19] Ikuhara, Y. Grain boundary atomic structures and light-element visualization in ceramics: Combination of Cs-corrected scanning transmission electron microscopy and first-principles calculations. *J. Electron Microsc.* **2011**, *60*, S173–S188.
- [20] Buban, J. P.; Matsunaga, K.; Chen, J.; Shibata, N.; Ching, W. Y.; Yamamoto, T.; Ikuhara, Y. Grain boundary strengthening in alumina by rare earth impurities. *Science* **2006**, *311*, 212–215.
- [21] Li, B. H.; Luo, L. J.; Xiao, T.; Hu, X. Y.; Lu, L.; Wang, J. B.; Tang, Y. W. Zn₃SnO₄-SnO₂ heterojunction nanocomposites for dye-sensitized solar cells. *J. Alloys Compd.* **2011**, *509*, 2186–2191.
- [22] Liu, S. Y.; Choy, W. C. H.; Jin, L.; Leung, Y. P.; Zheng, G. P.; Wang, J. B.; Soh, A. K. Triple-crystal zinc selenide nanobelts. *J. Phys. Chem. C* **2007**, *111*, 9055–9059.
- [23] Jin, L.; Choy, W. C. H.; Leung, Y. P.; Yuk, T. I.; Ong, H. C.; Wang, J. B. Synthesis and analysis of abnormal wurtzite ZnSe nanowheels. *J. Appl. Phys.* **2007**, *102*, 044302.
- [24] Tu, C. H.; Chang, C. C.; Wang, C. H.; Fang, H. C.; Huang, M. R. S.; Li, Y. C.; Chang, H. J.; Lu, C. H.; Chen, Y. C.; Wang, R. C. et al. Resistive memory devices with high switching endurance through single filaments in Bi-crystal CuO nanowires. *J. Alloys Compd.* **2014**, *615*, 754–760.
- [25] Liebscher, C. H.; Stoffers, A.; Alam, M.; Lymperakis, L.; Cojocaru-Mirédin, O.; Gault, B.; Neugebauer, J.; Dehm, G.; Scheu, C.; Raabe, D. Strain-induced asymmetric line segregation at faceted Si grain boundaries. *Phys. Rev. Lett.* **2018**, *121*, 015702.
- [26] Herbig, M.; Raabe, D.; Li, Y. J.; Choi, P.; Zaefferer, S.; Goto, S. Atomic-scale quantification of grain boundary segregation in nanocrystalline material. *Phys. Rev. Lett.* **2014**, *112*, 126103.
- [27] Deuermeier, J.; Wardenga, H. F.; Morasch, J.; Siol, S.; Nandy, S.; Calmeiro, T.; Martins, R.; Klein, A.; Fortunato, E. Highly conductive grain boundaries in copper oxide thin films. *J. Appl. Phys.* **2016**, *119*, 235303.
- [28] Younas, M.; Nadeem, M.; Idrees, M.; Akhtar, M. J. Jahn-Teller assisted polaronic hole hopping as a charge transport mechanism in CuO nanograins. *Appl. Phys. Lett.* **2012**, *100*, 152103.
- [29] Putjoso, T.; Manyum, P.; Yamwong, T.; Thongbai, P.; Maensiri, S. Effect of annealing on electrical responses of electrode and surface layer in giant-permittivity CuO ceramic. *Solid State Sci.* **2011**, *13*, 2007–2010.
- [30] Sheng, H. P.; Zheng, H.; Jia, S. F.; Li, L.; Cao, F.; Wu, S. J.; Han, W.; Liu, H. H.; Zhao, D. S.; Wang, J. B. Twin structures in CuO nanowires. *J. Appl. Cryst.* **2016**, *49*, 462–467.
- [31] Cao, F.; Jia, S. F.; Zheng, H.; Zhao, L. L.; Liu, H. H.; Li, L.; Zhao, L. G.; Hu, Y. M.; Gu, H. S.; Wang, J. B. Thermal-induced formation of domain structures in CuO nanomaterials. *Phys. Rev. Materials* **2017**, *1*, 053401.
- [32] Koch, C. T. Determination of core structure periodicity and point defect density along dislocations. Ph.D. Dissertation, Arizona State University, Tempe, AZ, USA, 2002.
- [33] Malis, T.; Cheng, S. C.; Egerton, R. F. EELS log-ratio technique for specimen-thickness measurement in the TEM. *J. Electron Microsc. Technol.* **1988**, *8*, 193–200.
- [34] Raebiger, H.; Lany, S.; Zunger, A. Origins of the p-type nature and cation deficiency in Cu₂O and related materials. *Phys. Rev. B* **2007**, *76*, 045209.
- [35] Wu, D. X.; Zhang, Q. M.; Tao, M. LSDA+U study of cupric oxide: Electronic structure and native point defects. *Phys. Rev. B* **2006**, *73*, 235206.
- [36] Sun, R.; Wang, Z. C.; Saito, M.; Shibata, N.; Ikuhara, Y. Atomistic mechanisms of nonstoichiometry-induced twin boundary structural transformation in titanium dioxide. *Nat. Commun.* **2015**, *6*, 7120.
- [37] Kingery, W. D. Plausible concepts necessary and sufficient for interpretation of ceramic grain-boundary phenomena: I, grain-boundary characteristics, structure, and electrostatic potential. *J. Am. Ceram. Soc.* **1974**, *57*, 1–8.
- [38] Bai, X. M.; Voter, A. F.; Hoagland, R. G.; Nastasi, M.; Uberuaga, B. P. Efficient annealing of radiation damage near grain boundaries via interstitial emission. *Science* **2010**, *327*, 1631–1634.
- [39] Leapman, R. D.; Grunes, L. A.; Fejes, P. L. Study of the L_{2,3} edges in the 3d transition metals and their oxides by electron-energy-loss spectroscopy with comparisons to theory. *Phys. Rev. B* **1982**, *26*, 614–635.
- [40] Waddington, W. G.; Rez, P.; Grant, I. P.; Humphreys, C. J. White lines in the L_{2,3} electron-energy-loss and X-ray absorption spectra of 3d transition metals. *Phys. Rev. B* **1986**, *34*, 1467–1473.
- [41] Graetz, J.; Ahn, C. C.; Ouyang, H.; Rez, P.; Fultz, B. White lines and d-band occupancy for the 3d transition-metal oxides and lithium transition-metal oxides. *Phys. Rev. B* **2004**, *69*, 235103.
- [42] Sparrow, T. G.; Williams, B. G.; Rao, C. N. R.; Thomas, J. M. L₃/L₂ white-line intensity ratios in the electron energy-loss spectra of 3d transition-metal oxides. *Chem. Phys. Lett.* **1984**, *108*, 547–550.

- [43] Ray, S. C. Preparation of copper oxide thin film by the sol–gel-like dip technique and study of their structural and optical properties. *Sol. Energy Mater. Sol. Cells* **2001**, *68*, 307–312.
- [44] Koffyberg, F. P.; Benko, F. A. A photoelectrochemical determination of the position of the conduction and valence band edges of p-type CuO. *J. Appl. Phys.* **1982**, *53*, 1173–1177.
- [45] Hardee, K. L.; Bard, A. J. Semiconductor electrodes: X. Photoelectrochemical behavior of several polycrystalline metal oxide electrodes in aqueous solutions. *J. Electrochem. Soc.* **1977**, *124*, 215–224.
- [46] Liao, Z. L.; Gauquelin, N.; Green, R. J.; Macke, S.; Gonnissen, J.; Thomas, S.; Zhong, Z. C.; Li, L.; Si, L.; van Aert, S. et al. Thickness dependent properties in oxide heterostructures driven by structurally induced metal–oxygen hybridization variations. *Adv. Funct. Mater.* **2017**, *27*, 1606717.
- [47] Kan, D.; Aso, R.; Sato, R.; Haruta, M.; Kurata, H.; Shimakawa, Y. Tuning magnetic anisotropy by interfacially engineering the oxygen coordination environment in a transition metal oxide. *Nat. Mater.* **2016**, *15*, 432–437.
- [48] Kresse, G.; Furthmüller, J. Efficiency of *ab-initio* total energy calculations for metals and semiconductors using a plane-wave basis set. *Comput. Mater. Sci.* **1996**, *6*, 15–50.
- [49] Kresse, G.; Furthmüller, J. Efficient iterative schemes for *ab initio* total-energy calculations using a plane-wave basis set. *Phys. Rev. B* **1996**, *54*, 11169–11186.
- [50] Mishra, A. K.; Roldan, A.; de Leeuw, N. H. CuO surfaces and CO₂ activation: A dispersion-corrected DFT+U study. *J. Phys. Chem. C* **2016**, *120*, 2198–2214.
- [51] Hu, J.; Li, D. D.; Lu, J. G.; Wu, R. Q. Effects on electronic properties of molecule adsorption on CuO surfaces and nanowires. *J. Phys. Chem. C* **2010**, *114*, 17120–17126.